– Supplementary Materials –

12µm-pitch electromechanical resonator for thermal sensing

Ludovic Laurent[1,2], Jean-Jacques Yon[1,2], Jean-Sébastien Moulet[1,2], Michael Roukes[3] and Laurent Duraffourg[1,2,]*

[1]Université Grenoble Alpes, F-38000 Grenoble, France.

[2]CEA, LETI, Minatec Campus, F-38054 Grenoble, France

[3]Departments of Physics, Applied Physics, and Bioengineering, Kavli Nanoscience Institute, California Institute of Technology, MC 149-33, Pasadena, California 91125, USA

[*]Corresponding Author, Email: laurent.duraffourg@cea.fr

APPENDIX A: FABRICATION PROCESS OF NEMS-BOLOMETERS

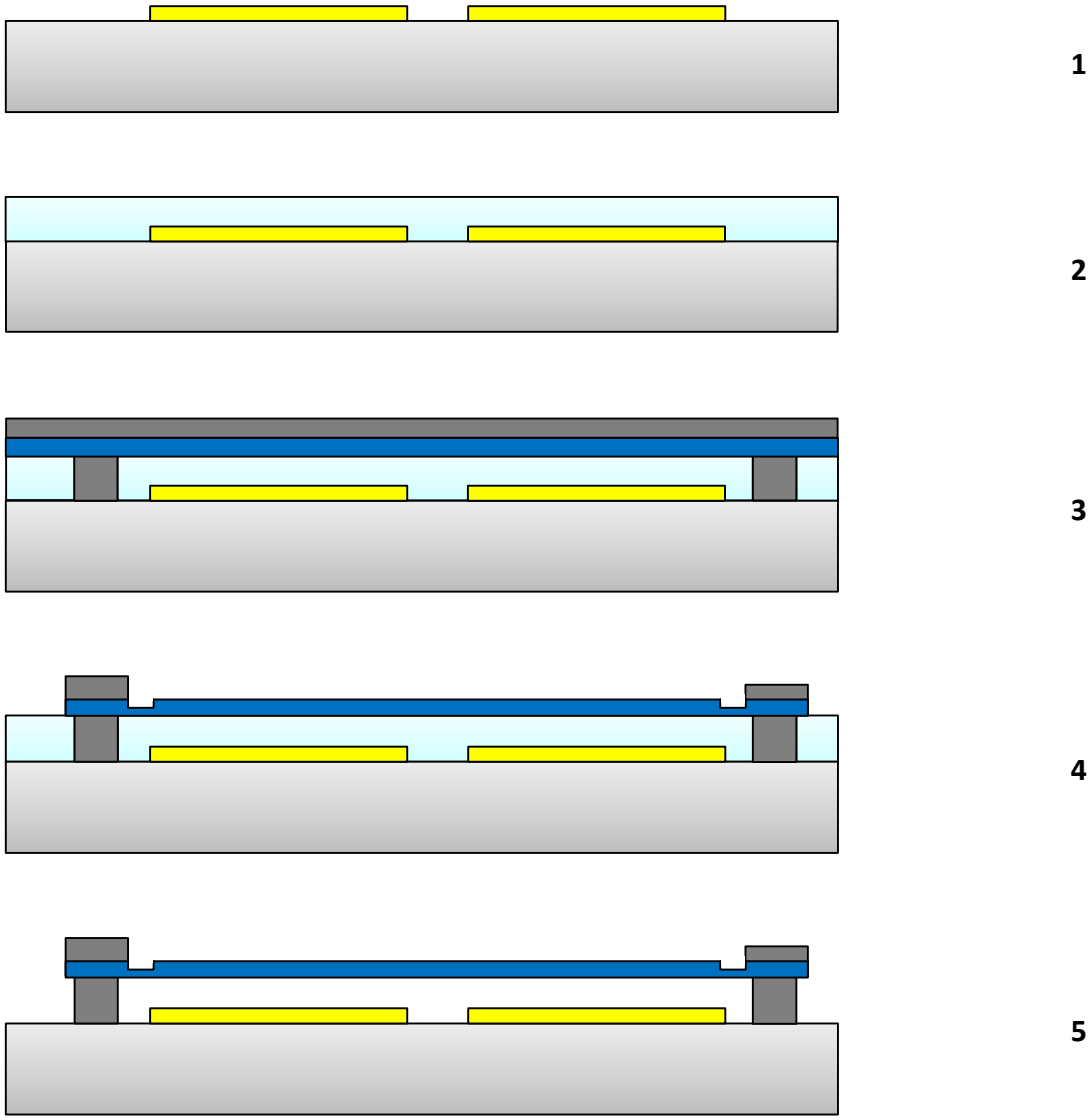

FIG. A.1: Schematic description of fabrication process

The fabrication process is described in FIG. A.1:

1. Deposition of 300 nm AlCu layer on a silicon substrate / strip lines / reflector wet etching.
2. 2 µm deposition of a polyimide layer
3. Opening of the polyimide layer to build up the metal studs
4. Whole wafer deposition of materials and dry etching

5. Plasma O2 releasing.

APPENDIX B: ELECTROMECHANICAL MODEL

θ_0 is the angle between the paddle and the fixed electrode. The polar coordinates are used here (see FIG. A.2). The origin is taken at the intersection between substrate and paddle continuation. We take W_p as the paddle width and L_p as its length (outside the plane here). g is the initial gap between paddle and electrode. We consider here a fixed electrode longer than the effective paddle length, such as the capacitive signal is limited by paddle length.

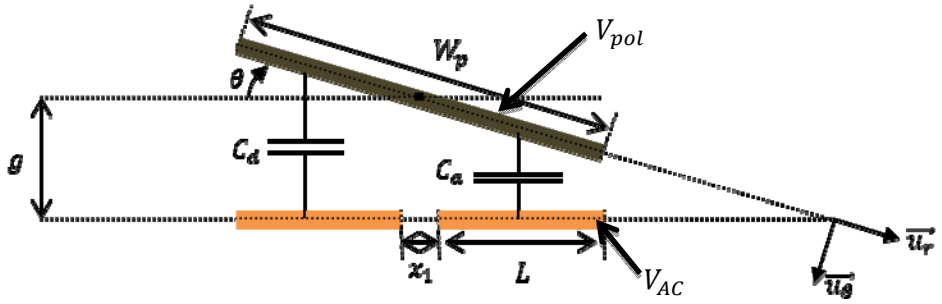

FIG. A.2: Scheme of electrostatic transduction and detection.

For $0 < \theta < \theta_0$, we have a free space of charge, thus $div\,\vec{E} = \rho/\varepsilon_0 = 0$. By symmetry, $V(r,\theta,\varphi) = V(\theta)$. Therefore, $\text{div}\,\vec{E} = \frac{1}{r}\frac{d^2V}{d\theta^2} = 0$. With the boundary conditions $V(0) = V_{AC}$ and $V(\theta_0) = V_{pol}$, we can deduce $\frac{\partial V}{\partial \theta} = \frac{V_{pol}-V_{AC}}{\theta_0}$. The electrical field between the electrodes is:

$$\vec{E} = -\overrightarrow{\text{grad}}(V) = -\frac{1}{r}\frac{V_{pol} - V_{AC}}{\theta_0}\overrightarrow{u_\theta} \tag{A.1}$$

The charge across a surface electrode $d\vec{S}$ is thus $dq = \varepsilon_0\vec{E}.d\vec{S} = \varepsilon_0 E dS$. Finally, integrating over the length of the paddle (for $\theta = \theta_0$)

$$q = \varepsilon_0 L_p \frac{V_{AC} - V_{pol}}{\theta_0}\int_{-\left(\frac{g}{\sin(\theta_0)}-\frac{W_p}{2}\right)}^{-\left(\frac{g}{\sin(\theta_0)}-\frac{x_1/2}{\cos(\theta_0)}\right)}\frac{dr}{r} \tag{A.2}$$

Considering the definition of electrical capacitance $q = C \times U$, the capacitance between the two electrodes tilted by an angle θ is:

$$C_a(\theta) = \frac{\varepsilon_0 L_p}{\theta} \ln\left(\frac{g - \frac{x_1}{2}\tan(\theta)}{g - \frac{W_p}{2}\sin(\theta)}\right) \tag{A.3}$$

Likewise, the capacitance between the other electrode and the paddle is:

$$C_d(\theta) = \frac{\varepsilon_0 L_p}{\theta} \ln\left(\frac{g + \frac{W_p}{2}\sin(\theta)}{g + \frac{x_1}{2}\tan(\theta)}\right) \tag{A.4}$$

Defining the later as the detection electrode and the other as the actuation one, $\sin(\theta_{max}) = \frac{g}{W_p/2}$ and $C_0 = \varepsilon_0 \frac{L_p W_p/2}{g}$:

$$\begin{aligned} C_a(\theta) &= C_0 \frac{\sin(\theta_{max})}{\theta} \ln\left(\frac{1 - \frac{x_1}{W_p}\frac{\tan(\theta)}{\sin(\theta_{max})}}{1 - \frac{\sin(\theta)}{\sin(\theta_{max})}}\right) \\ C_d(\theta) &= C_0 \frac{\sin(\theta_{max})}{\theta} \ln\left(\frac{1 + \frac{\sin(\theta)}{\sin(\theta_{max})}}{1 + \frac{x_1}{W_p}\frac{\tan(\theta)}{\sin(\theta_{max})}}\right) \end{aligned} \tag{A.5}$$

Now, some approximations can be made in order to simplify these expressions. Assuming $x_1 \ll W_p$ and being in the regime of small amplitudes, Eq. (A.5) becomes:

$$\begin{aligned} C_a(\theta) &\approx -C_0 \frac{\theta_{max}}{\theta} \ln\left(1 - \frac{\theta}{\theta_{max}}\right) \\ C_d(\theta) &\approx C_0 \frac{\theta_{max}}{\theta} \ln\left(1 + \frac{\theta}{\theta_{max}}\right) \end{aligned} \tag{A.6}$$

A Taylor expansion of these expressions leads to:

$$C_a(\theta) \sim C_0 \left(1 + \frac{1}{2}\frac{\theta}{\theta_{max}} + \frac{1}{3}\left(\frac{\theta}{\theta_{max}}\right)^2 + \frac{1}{4}\left(\frac{\theta}{\theta_{max}}\right)^3\right)$$

$$C_d(\theta) \sim C_0 \left(1 - \frac{1}{2}\frac{\theta}{\theta_{max}} + \frac{1}{3}\left(\frac{\theta}{\theta_{max}}\right)^2 - \frac{1}{4}\left(\frac{\theta}{\theta_{max}}\right)^3\right) \quad \text{(A.7)}$$

The accuracy of several approximations on capacitance change $\delta C = C_d - C_0$ with deflection angle is presented in FIG. A.3. We observe that the linear approximation holds until the deflection reaches 2.5°.

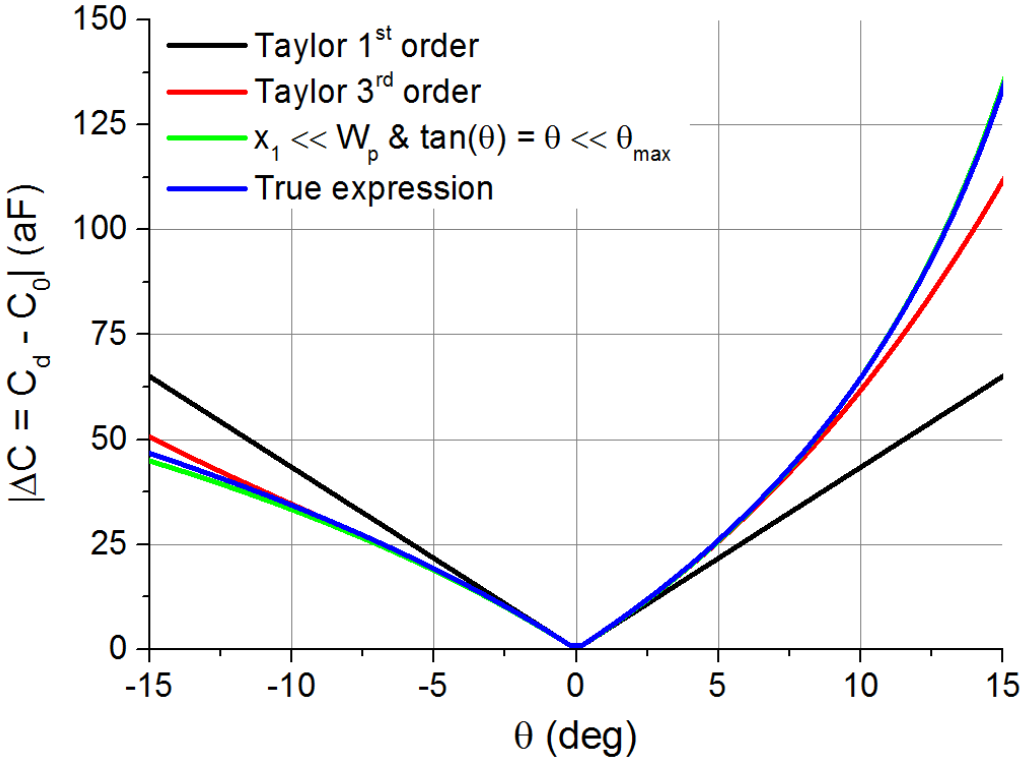

FIG. A.3: Motional capacitance as a function of deflection angle for various geometrical approximations.

Finally the electrical torque is defined by:

$$T_e(\theta) = \frac{1}{2}\frac{dC}{d\theta}U^2 \quad \text{(A.8)}$$

With:

$$\frac{dC_a}{d\theta} = \frac{C_0}{\theta}\left(\frac{\theta_{max}}{\theta}\ln\left(1-\frac{\theta}{\theta_{max}}\right)+\frac{1}{1-\frac{\theta}{\theta_{max}}}\right)$$
$$\frac{dC_d}{d\theta} = \frac{C_0}{\theta}\left(-\frac{\theta_{max}}{\theta}\ln\left(1+\frac{\theta}{\theta_{max}}\right)+\frac{1}{1+\frac{\theta}{\theta_{max}}}\right) \quad \text{(A.9)}$$

After Taylor's development, expressions become:

$$\frac{dC_a}{d\theta} \sim C_0\left(\frac{1}{2}\frac{1}{\theta_{max}}+\frac{2}{3}\frac{\theta}{\theta_{max}^2}+\frac{3}{4}\frac{\theta^2}{\theta_{max}^3}+\frac{4}{5}\frac{\theta^3}{\theta_{max}^4}\right)$$
$$\frac{dC_d}{d\theta} \sim C_0\left(-\frac{1}{2}\frac{1}{\theta_{max}}+\frac{2}{3}\frac{\theta}{\theta_{max}^2}-\frac{3}{4}\frac{\theta^2}{\theta_{max}^3}+\frac{4}{5}\frac{\theta^3}{\theta_{max}^4}\right) \quad \text{(A.10)}$$

Thus, the total electrical torque applied to the paddle is:

$$T_e = \frac{1}{2}\frac{dC_a}{d\theta}(V_{AC}-V_{pol})^2+\frac{1}{2}\frac{dC_d}{d\theta}(V_{pol})^2$$
$$\Leftrightarrow T_e = \frac{1}{2}\frac{dC_a}{d\theta}V_{AC}^2-\frac{dC_a}{d\theta}V_{AC}V_{pol}+\frac{1}{2}\left(\frac{dC_d}{d\theta}+\frac{dC_a}{d\theta}\right)V_{pol}^2 \quad \text{(A.11)}$$

Assuming a sinusoidal actuation voltage $V_{AC}(t) = V_{AC}\cos\left(\frac{\omega}{2}t\right)$, and $V_{AC} \ll V_{pol}$:

$$T_e \sim \frac{C_0}{2}\left\{\frac{V_{AC}^2}{2}\cos(\omega t)\left(\frac{1}{2}\frac{1}{\theta_{max}}+\frac{2}{3}\frac{\theta}{\theta_{max}^2}\right)-2V_{AC}V_{pol}\cos\left(\frac{\omega}{2}t\right)\left(\frac{1}{2}\frac{1}{\theta_{max}}+\frac{2}{3}\frac{\theta}{\theta_{max}^2}\right)\right.$$
$$\left.+V_{pol}^2\left(\frac{4}{3}\frac{\theta}{\theta_{max}^2}+\frac{8}{5}\frac{\theta^3}{\theta_{max}^4}\right)\right\} \quad \text{(A.12)}$$

We can now have an idea of the signal level for a given torque. Indeed, the harmonic damped oscillator equation is:

$$J\ddot{\theta} + b\dot{\theta} + \kappa\theta = T_e \tag{A.13}$$

With $J = \frac{M_p W_p^2}{12}$ the moment of inertia of the paddle, assuming the inertia moment of rods negligible. The torsional stiffness of these rods κ, is defined by :

$$\kappa = \frac{2GI_r}{L_r} \tag{A.14}$$

With G the shear modulus $G = \frac{E}{2(1+\nu)}$ and I_r the torsional quadratic moment of the rectangular suspended rods (factor 2 is due to the two rods):

$$I_r = \begin{cases} t_r w_r^3 \left(\frac{1}{3} - 0.21\frac{w_r}{t_r}\left(1 - \frac{1}{12}\frac{w_r^4}{t_r^4}\right)\right) if\ t_r > w_r \\ w_r t_r^3 \left(\frac{1}{3} - 0.21\frac{t_r}{w_r}\left(1 - \frac{1}{12}\frac{t_r^4}{w_r^4}\right)\right) if\ w_r > t_r\ (our\ case) \end{cases} \tag{A.15}$$

The substitution of (A.12) into (A.13) leads to the paddle motion equation:

$$\ddot{\theta} + \alpha\dot{\theta} + \beta\theta + \delta\theta^3 = \frac{1}{J}(T_0 + T_1(\omega) + T_2(\omega/2))$$

$$T_0 = \frac{C_0}{2}\frac{V_{AC}^2}{4\theta_{max}}, T_1 = \frac{C_0}{2}\frac{V_{AC}^2}{4\theta_{max}}cos(\omega t), T_2 = -\frac{C_0}{2}\frac{V_{AC}V_{pol}}{\theta_{max}}cos\left(\frac{\omega}{2}t\right)$$

$$\omega_0 = \sqrt{\frac{\kappa}{J}}$$

$$\alpha = \frac{\omega_0}{Q} \tag{A.16}$$

$$\beta = \omega_0^2 - \frac{1}{J}\frac{C_0}{2}\frac{1}{\theta_{max}^2}\left(\frac{4}{3}V_{pol}^2 + \frac{1}{3}V_{AC}^2\cos(\omega t) - \frac{4}{3}V_{AC}V_{pol}\cos\left(\frac{\omega}{2}t\right)\right)$$

$$\delta = -\frac{1}{J}\frac{C_0}{4}\frac{8}{5}\frac{V_{pol}^2}{\theta_{max}^4}$$

One can notice that this expression looks like a Duffing equation because of the cubic term. The harmonic terms in the effective stiffness can lead to sub-harmonic excitations. We will not focus on the nonlinear terms in this paper, we will therefore assume a linear operation in the following sections. Thus, after few tedious mathematical manipulations the resonance angle will be:

$$\theta_r = C_0\frac{V_{AC}^2}{8\theta_{max}}\frac{Q}{\sqrt{\kappa^2 - \frac{4}{3}\frac{C_0}{2}\frac{\kappa V_{pol}^2}{\theta_{max}^2}}} \tag{A.17}$$

With Q the quality factor.

In the approximation of small amplitudes, the capacitance variation is:

$$\delta C(\theta_r) = C_0\frac{1}{2}\frac{\theta_r}{\theta_{max}} \tag{A.18}$$

I.e. 11 aF assuming a deflection of 2.5° at resonance. The nonlinear electrostatic terms in Eq. (A.16) would be one source of nonlinear behavior.

APPENDIX C: THEORETICAL NOISE STUDY

1. Radiation noise

The minimal optical power theoretically detectable by our system is the exchanged radiative power between the bolometer and its close environment. This noise has a similar source as the so-called phonon noise – i.e. thermal fluctuations. It occurs when power exchanges between the bolometer and its environment are dominated by radiation. The fluctuations of bolometer temperature due to radiation noise will thus create fluctuations in the radiative exchanges leading to additive temperature noise. Depending on paddle materials, thickness and/or size this so-called radiation noise could be greater than phonon or thermomechanical noise. The power spectral density of this emission/absorption phenomena for low frequency (compared to photon arrival rate) is a white noise [1]:

$$S_{P_{rad}} = 4k_B T^2 G_{rad} \text{ where } G_{rad} = 4\left(2\beta A_p\right)\varepsilon\sigma_{Stef}T^3 \tag{A.19}$$

Where σ_{Stef} is the Stefan-Boltzmann constant, ε the bolometer emissivity coefficient with this environment (usually evaluated to 0.8 [1]) and β the fill factor. G_{rad} is accounted for a bolometer undergoing the same temperature at his both sides (i.e. 300 K). The temperature spectral density is then:

$$S_T(\omega) = \frac{4k_B T^2}{G_{rad}} \frac{1}{1 + \omega^2 {\tau_{th}}^2} \tag{A.20}$$

Where $\tau_{th} = C/G_{rad}$. Finally, simplifying this expression with the equivalent noise bandwidth (ENBW) of a first order filter, the noise equivalent power is:

$$NEP_{rad} = \begin{cases} \sqrt{4G_{rad}k_B T^2 * BW} \text{ where } BW < BW_{th} = \dfrac{1}{4\tau_{th}} \\ G_{rad}\sqrt{\dfrac{k_B T^2}{C}} \text{ where } BW > BW_{th} \end{cases} \tag{A.21}$$

Where BW is the integration bandwidth $\sim 1/4\tau_{integration}$ for a 1st order low pass filter. Considering $\beta A_p = 0.8 \times (12\ \mu m)^2, C = 26.10^{-12}\ J/K, G = 5 \times 10^{-8}\ W/K$, a total NEP of 1.8 pW is estimated. It is much lower than the phonon noise in our case (estimated to 11 pW).

2. Thermomechanical noise

The loss energy inside the resonator gives rise to unwanted random paddle motion because of ambient thermal bath. This amplitude noise is called thermomechanical noise (or Brownian noise). The motion spectral density is given by:

$$-\infty < \omega < \infty \qquad S_\theta(\omega) = \frac{2k_B T}{Q\kappa}\omega_0^3 \frac{1}{({\omega_0}^2 - \omega^2)^2 + \left(\frac{\omega\omega_0}{Q}\right)^2} \tag{A.22}$$

We provided a global analytical expression of the thermomechanical noise over a bandwidth higher than ω_0/Q:

$$\langle\theta^2\rangle = \frac{1}{2\pi}\int_{\omega_0-\frac{\Delta\omega}{2}}^{\omega_0+\frac{\Delta\omega}{2}} S_\theta(\omega)d\omega$$

$$\Leftrightarrow \langle\theta^2\rangle = \frac{1}{2\pi}\int_{\omega_0-\frac{\Delta\omega}{2}}^{\omega_0+\frac{\Delta\omega}{2}} \frac{2k_B T}{Q\kappa}\omega_0^3 \frac{1}{({\omega_0}^2 - \omega^2)^2 + \left(\frac{\omega\omega_0}{Q}\right)^2} d\omega \tag{A.23}$$

$$\text{Let's be } X = \frac{\omega}{\omega_0} \rightarrow d\omega = \omega_0 dX$$

$$\Leftrightarrow \langle\theta^2\rangle = \frac{1}{2\pi}\frac{2k_B T}{Q\kappa}\int_{1-\frac{\Delta\omega}{2\omega_0}}^{1+\frac{\Delta\omega}{2\omega_0}} \frac{dX}{(1-X^2)^2 + \left(\frac{X}{Q}\right)^2}$$

Considering the integral I and the polynomial P:

$$I = \int_{1-\frac{\Delta\omega}{2\omega_0}}^{1+\frac{\Delta\omega}{2\omega_0}} \frac{dX}{(1-X^2)^2 + \left(\frac{X}{Q}\right)^2} \qquad P[X] = (1-X^2)^2 + \left(\frac{X}{Q}\right)^2 \tag{A.24}$$

To calculate I, $P[X]$ needs to be simplified into a product of first order polynomials – to this end we have to find the roots. λ_1 is one of them. As P is symmetric, $-\lambda_1$ is also a solution of $P[X] = 0$. Since the coefficient of P are real $\overline{\lambda_1}$ and $\overline{-\lambda_1}$ are solutions. We write $u = X^2$:

$$P[\lambda] = 0 \iff u^2 + u\frac{1-2Q^2}{Q^2} + 1 = 0$$
$$\Delta = \frac{(1-2Q^2)^2}{Q^4} - 4 = \frac{1-4Q^2}{Q^4} = j^2\frac{4Q^2-1}{Q^4} \tag{A.25}$$

Thus:

$$u_{1,2} = \frac{1}{2Q^2}\left(2Q^2 - 1 \mp j\sqrt{4Q^2-1}\right) \tag{A.26}$$

We can observe that $|u_{1,2}| = 1$. If $\lambda_1 = a + jb$, we have:

$$\lambda_1^2 = u_1 \iff \begin{cases} a^2 - b^2 = \frac{1}{2Q^2}(2Q^2-1) \\ a^2 + b^2 = 1 \end{cases}$$
$$\Rightarrow \begin{cases} a = \frac{1}{2Q}\sqrt{4Q^2-1} \\ b = \frac{1}{2Q} \end{cases} \tag{A.27}$$

Therefore $\lambda_1 = \frac{1}{2Q}\left(\sqrt{4Q^2-1} + j\right)$. We can now rewrite $\frac{1}{P[X]}$:

$$\frac{1}{P(X)} = \frac{1}{8j\mathrm{Re}(\lambda_1)\mathrm{Im}(\lambda_1)|\lambda_1|^2}\left(\frac{\overline{\lambda_1}}{X-\lambda_1} - \frac{\lambda_1}{X-\overline{\lambda_1}} - \frac{\overline{\lambda_1}}{X+\lambda_1} + \frac{\lambda_1}{X+\overline{\lambda_1}}\right) \tag{A.28}$$

Gathering conjugate terms, (A.28) becomes:

$$\frac{1}{P(X)} = \frac{1}{8\mathrm{Re}(\lambda_1)|\lambda_1|^2}\left(-\frac{2X-4\mathrm{Re}(\lambda_1)}{X^2-2\mathrm{Re}(\lambda_1)X+|\lambda_1|^2} + \frac{2X+4\mathrm{Re}(\lambda_1)}{X^2+2\mathrm{Re}(\lambda_1)X+|\lambda_1|^2}\right)$$

$$= \frac{1}{8\mathrm{Re}(\lambda_1)|\lambda_1|^2}\left(-\frac{2X-2\mathrm{Re}(\lambda_1)}{X^2-2\mathrm{Re}(\lambda_1)X+|\lambda_1|^2} + \frac{2X+2\mathrm{Re}(\lambda_1)}{X^2+2\mathrm{Re}(\lambda_1)X+|\lambda_1|^2}\right. \tag{A.29}$$

$$\left. + \frac{2\mathrm{Re}(\lambda_1)}{\mathrm{Im}^2(\lambda_1)}\left(\frac{1}{\left(\frac{X-\mathrm{Re}(\lambda_1)}{\mathrm{Im}(\lambda_1)}\right)^2+1} + \frac{1}{\left(\frac{X+\mathrm{Re}(\lambda_1)}{\mathrm{Im}(\lambda_1)}\right)^2+1}\right)\right)$$

The integral of the function (A.29) over the interval $\left[1-\frac{\Delta\omega}{2\omega_0}; 1+\frac{\Delta\omega}{2\omega_0}\right]$ is:

$$I = \frac{1}{8\mathrm{Re}(\lambda_1)|\lambda_1|^2}\left(\left[\ln\left(\frac{X^2+2\mathrm{Re}(\lambda_1)X+|\lambda_1|^2}{X^2-2\mathrm{Re}(\lambda_1)X+|\lambda_1|^2}\right)\right]_{1-\frac{\Delta\omega}{2\omega_0}}^{1+\frac{\Delta\omega}{2\omega_0}}\right.$$

$$+ \frac{2Re(\lambda_1)}{Im(\lambda_1)}\left(\left[\arctan\left(\frac{X+2\mathrm{Re}(\lambda_1)}{\mathrm{Im}(\lambda_1)}\right)\right]_{1-\frac{\Delta\omega}{2\omega_0}}^{1+\frac{\Delta\omega}{2\omega_0}}\right. \tag{A.30}$$

$$\left.\left. + \left[\arctan\left(\frac{X-2\mathrm{Re}(\lambda_1)}{\mathrm{Im}(\lambda_1)}\right)\right]_{1-\frac{\Delta\omega}{2\omega_0}}^{1+\frac{\Delta\omega}{2\omega_0}}\right)\right)$$

We replace λ_1 by its expression (A.27):

$$I = \frac{2Q}{8\sqrt{4Q^2-1}}\left(\left[\ln\left(\frac{X^2+\frac{1}{Q}\sqrt{4Q^2-1}X+1}{X^2-\frac{1}{Q}\sqrt{4Q^2-1}X+1}\right)\right]_{1-\frac{\Delta\omega}{2\omega_0}}^{1+\frac{\Delta\omega}{2\omega_0}}\right.$$
$$+ 2\sqrt{4Q^2-1}\left[\arctan\left(2QX+2\sqrt{4Q^2-1}\right)\right.$$
$$\left.\left.+ \arctan\left(2QX-2\sqrt{4Q^2-1}\right)\right]_{1-\frac{\Delta\omega}{2\omega_0}}^{1+\frac{\Delta\omega}{2\omega_0}}\right) \quad \text{(A.31)}$$

This expression can be further simplified because $4Q^2 \gg 1$

$$I = \frac{1}{8}\left(\left[\ln\left(\frac{X^2+2X+1}{X^2-2X+1}\right)\right]_{1-\frac{\Delta\omega}{2\omega_0}}^{1+\frac{\Delta\omega}{2\omega_0}}\right.$$
$$\left.+ 4Q\left[\arctan\big(2Q(X+2)\big)+\arctan\big(2Q(X-2)\big)\right]_{1-\frac{\Delta\omega}{2\omega_0}}^{1+\frac{\Delta\omega}{2\omega_0}}\right) \quad \text{(A.32)}$$

We compute the thermomechanical noise as a function of noise bandwidth $\Delta\omega$ from (A.32). The results are reported in FIG. A.4 for a nominal resonator depicted in TABLE I ($Q = 1800$, $f_0 = 1.1\,MHz$ and $\kappa = 1.8 \times 10^{-11}\,N.m$). We compare this exact computation from usual small bandwidth approximation and total thermomechanical noise for an infinite bandwidth. We observe that our development is of particular interest from 200 Hz to 7 kHz noise-bandwidth, a relevant range for imaging applications.

Then, taking the limit $\Delta\omega \to \infty$, we observe that:

$$\lim_{\Delta\omega\to\infty}\left[\ln\left(\frac{X^2+\frac{1}{Q}\sqrt{4Q^2-1}X+1}{X^2-\frac{1}{Q}\sqrt{4Q^2-1}X+1}\right)\right]_{1-\frac{\Delta\omega}{2\omega_0}}^{1+\frac{\Delta\omega}{2\omega_0}} = \lim_{\Delta\omega\to\infty}\ln(1) = 0 \quad \text{(A.33)}$$

$$\lim_{\Delta\omega\to\infty}\left(4Q\left[\arctan\left(2Q(X+2)\right)+\arctan\left(2Q(X-2)\right)\right]_{1-\frac{\Delta\omega}{2\omega_0}}^{1+\frac{\Delta\omega}{2\omega_0}}\right)$$

$$=\ 4Q\left(\frac{\pi}{2}-\left(-\frac{\pi}{2}\right)+\frac{\pi}{2}-\left(-\frac{\pi}{2}\right)\right)=8\pi Q$$

And thus

$$\lim_{\Delta\omega\to\infty}\langle\theta^2\rangle=\frac{1}{2\pi}\frac{2k_BT}{Q\kappa}\lim_{\Delta\omega\to\infty}I=k_BT/\kappa$$

This expression could be found by the equipartition energy principle:

$$\left\langle\frac{1}{2}J\dot{\theta}^2\right\rangle=\frac{1}{2}k_BT$$

$$\Leftrightarrow J\omega_0^2\langle\theta^2\rangle=k_BT \qquad \text{(A.34)}$$

$$\Leftrightarrow\langle\theta^2\rangle=\frac{k_BT}{\kappa}$$

It can be observed that for a rolling-shutter read-out (red star), the approximation is no longer true and overestimated the noise by a factor 5.

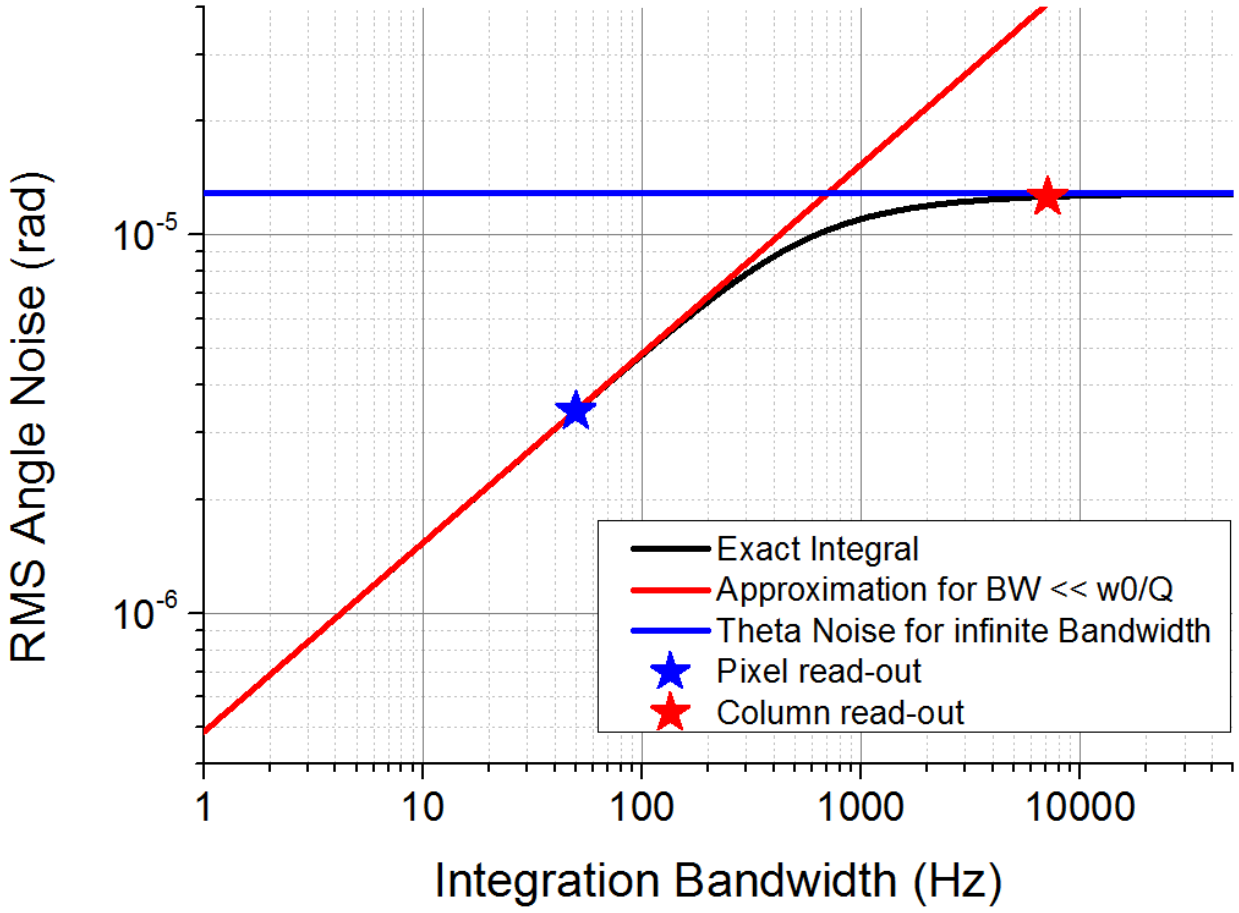

FIG. A.4: Thermomechanical noise (expressed in angle) integrated as a function of noise bandwidth (black curve): The constant approximation (red curve), true for $\Delta\omega \ll \omega_0/Q$ is also plotted as well as the noise for an infinite bandwidth (blue curve). We simulate the thermomechanical noise for a nominal device depicted in TABLE I ($f_0 = 1.1\ MHz$, $Q = 1800$ and $\kappa = 1.8 \times 10^{-11}\ N.m$).

APPENDIX D: EXPERIMENTAL DETECTION SCHEME

1. Amplifier and electronical noise

Two main techniques allow to detect a capacitive signal. In the first case, the carriers into the capacitance are set and we measure the voltage variation. In the second approach, the voltage is set and the charge carriers are measured. This technique requires a dedicated electronics, however, the signal to detect does not depend anymore on the downstream capacitance. Hence, if carefully designed, the intermediate circuit can substantially improve the signal to noise ratio.

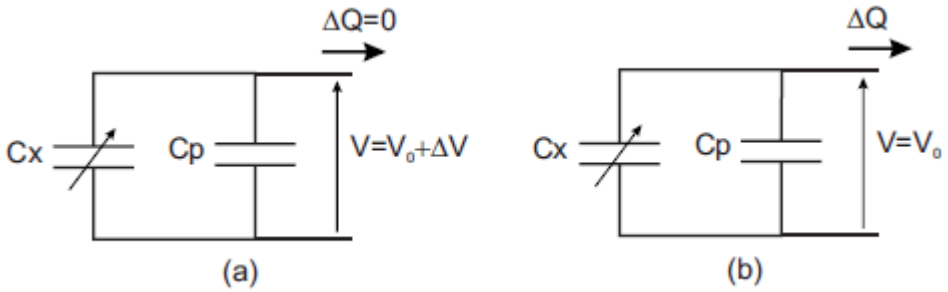

FIG. A.5: Capacitance detection: 2 approaches. (a) charge is constant (large output impedance) (b) low impedance measurements (charge variation is measured) [2].

We read the current with a feedback capacitance C_{C2V} instead of a resistor to minimize the background. Thus, the output voltage will be:

$$V_{out} = V_{pol}\frac{\delta C(\theta_r)}{C_{C2V}} \tag{A.35}$$

Where $\delta C(\theta_r)$ is capacitance variation resulting from the motion of the paddle. C_{C2V} must be chosen as low as possible to maximize the output signal but should stay high enough to avoid unwanted effects due to parasitic capacitances (and $k_B T/C$ noise). As shown in FIG. A.3, we notice that $\delta C(\theta_r)$ is not symmetrical for $\theta_r > 2.5°$. As a consequence, the sinusoidal component of V_{out} is not centered on the origin. Since our lock-in amplifier removes the DC component of the signal, the detected signal reads:

$$V_{out} = V_{pol}\frac{\left(\delta C(\theta_r) - \delta C(-\theta_r)\right)}{2C_{C2V}} \tag{A.36}$$

We choose a 1 pF feedback capacitance in parallel with a 10 GOhm resistor which avoid saturation of the output signal caused by DC current. FIG. A.6 describes the main elements of our circuit with the main sources of noise added.

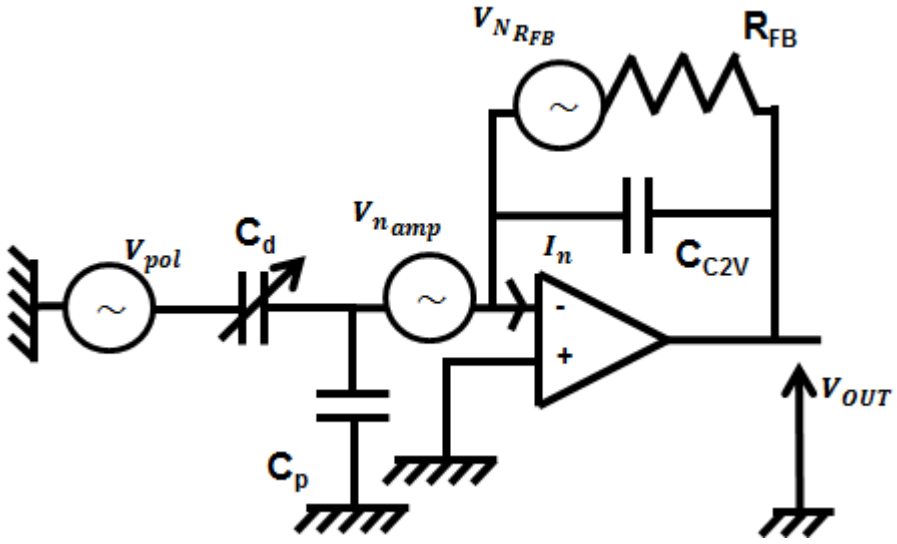

FIG. A.6 : Transimpedance circuit and main sources of noise. $\boldsymbol{V_{n_{amp}}}$ accounts for the input voltage noise of the amplifier and $\boldsymbol{I_n}$ for the input current noise. Depending on applications, a trade off exists between these two values, and determines the suitable transistor technology. Here, a low $\boldsymbol{V_{n_{amp}}}$ and low input capacitance is highly desirable. Usually, JFET transistors fill these requirements.

The mobile electrode is modeled by the variable capacitance C_d. C_p accounts for the total input capacitance of the amplifier. This set up behaves like a high band filter [3]:

$$V_{out} = V_{pol}\frac{C_d}{C_{C2V}}\left|\frac{1}{\left(1-j\frac{f_c}{f}\right)\left(1+j\frac{f}{f_{CO}\frac{C_{C2V}}{C_p}}\right)}\right| \qquad \text{(A.37)}$$

Where f_{CO} is the high frequency cut-off of the amplifier and $f_c = \frac{1}{2\pi R_{FB}C_{C2V}}$ the frequency at -3dB of the RC filter.

The noises are:

$$V_{tot} = \sqrt{V_{n_{R_f}}^2 + V_{n_{I_n}}^2 + V_{n_{amp}}^2} \text{ with}$$

$$V_{n_{amp}} = V_n \left| 1 + \frac{C_p}{C_{C2V}} \frac{1}{\left(1 - j\frac{f_c}{f}\right)} \right| \left| \frac{1}{\left(1 + j\frac{C_p}{C_{C2V}}\frac{f}{f_{CO}}\right)} \right|$$

$$V_{n_{R_{FB}}} = \sqrt{4k_B T R_{FB}} \left| \frac{1}{1 + j\frac{f}{f_c}} \right| \tag{A.38}$$

$$V_{n_{I_n}} = R_{FB} I_n \left| \frac{1}{1 + j\frac{f}{f_c}} \right|$$

We use here a ADA4817 from Analog Devices with the following noise performance:

TABLE A.1. Main Noise characteristics of ADA 4817 amplifier [4]

	$V_n\ (nV/\sqrt{Hz})$	$I_n(fA/\sqrt{Hz})$	$f_{CO}(MHz)$	$C_{in}(pF)$
ADA4817	4	2.5	1050	1.3

We embedded the circuit as close as possible to the detection electrode. We believe thereby that the input capacitance will be only limited by the input capacitance of the amplifier.

Adding the contribution of our lock-in ($\mathbf{5}\,\boldsymbol{nV/\sqrt{Hz}}$), a noise floor of $\mathbf{10}\,\boldsymbol{nV/\sqrt{Hz}}$ is theoretically reachable. Unfortunately, we experimentally observed a noise floor of $\mathbf{40}\,\boldsymbol{nV/\sqrt{Hz}}$ (

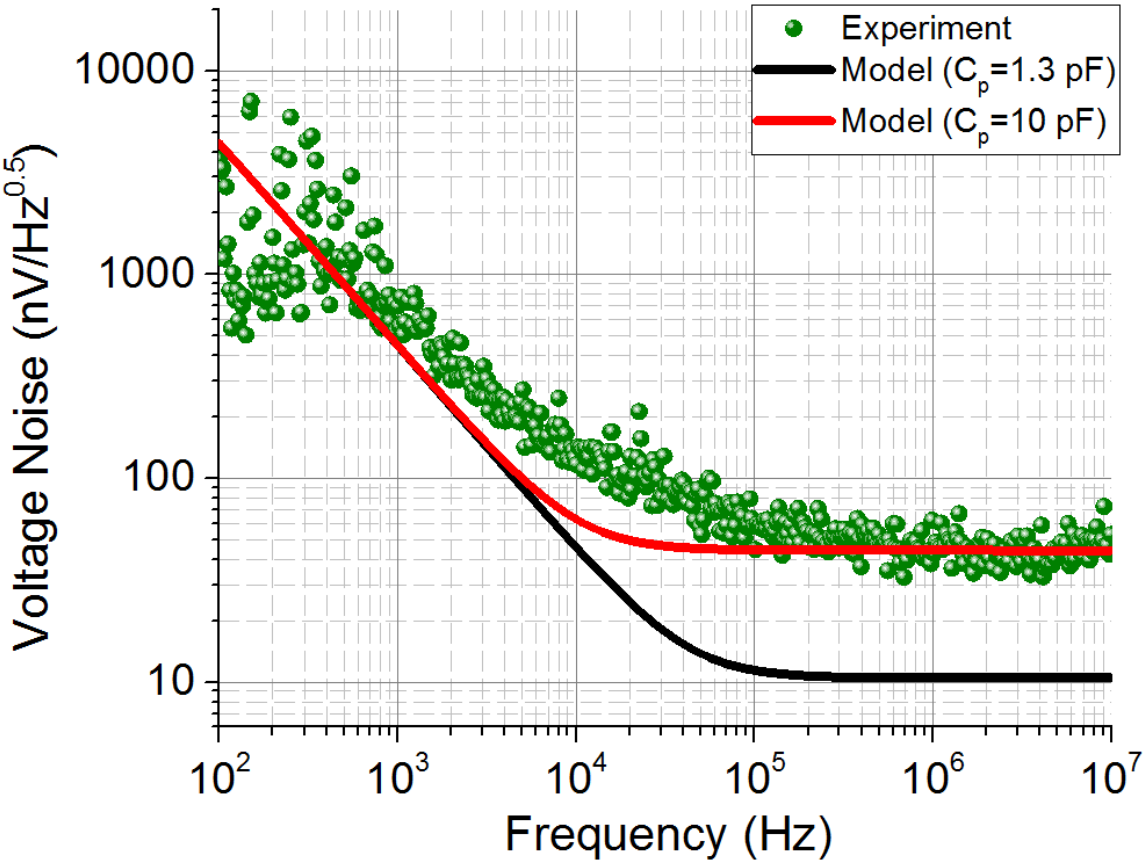

FIG. **A.7**). We believe that this discrepancy would be corrected by co-integrating this circuit. The co-integration will remove the unwanted capacity due to bonding pads and wires [5]

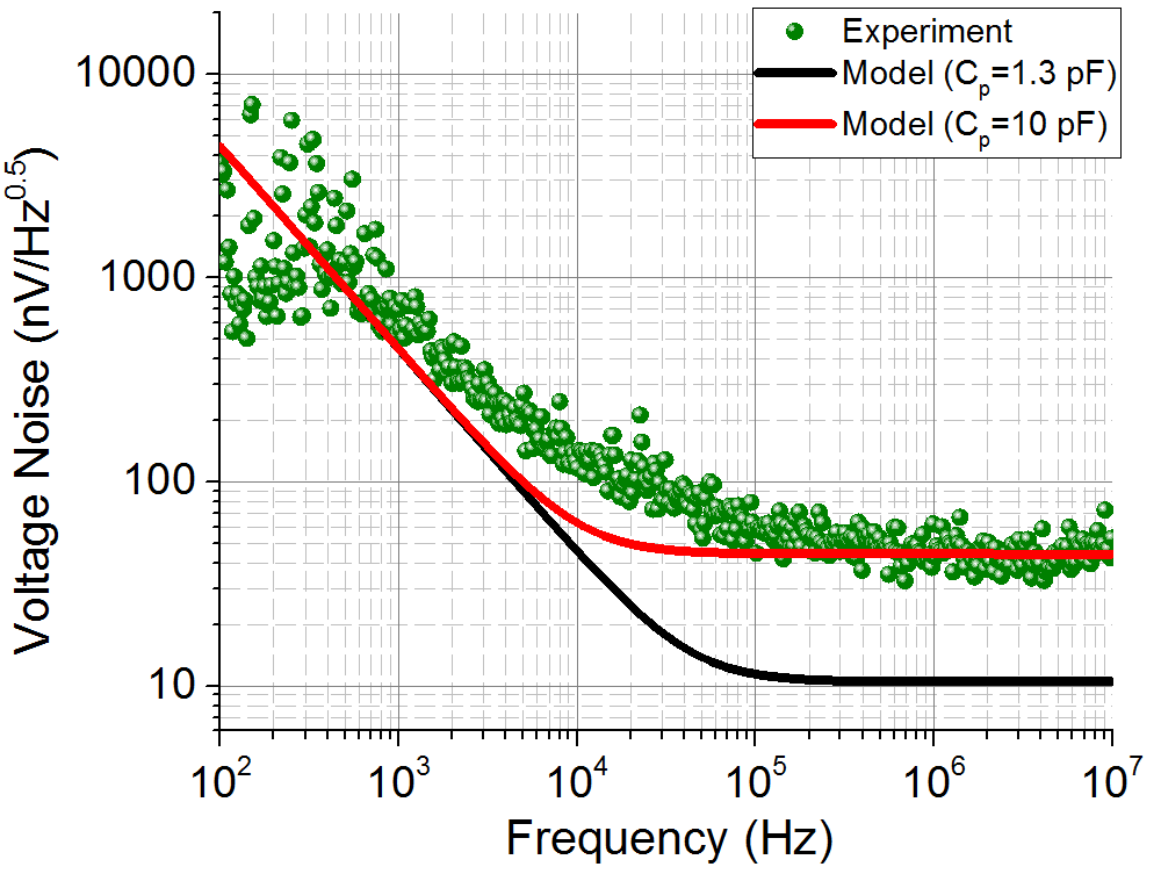

FIG. A.7 : Electrical noise spectrum. The low frequency is set at 100 kHz because of the 1/f corner of the AD4817 (only white noise is included in our model). The black line is the simulated noise for input capacitance equals to the amplifier input capacitance. The red line is a fit of the experimental noise floor (10 pF input capacitance). The discrepancy below 100 kHz likely occurs because of 1/f noise from amplifier which is not included in our model.

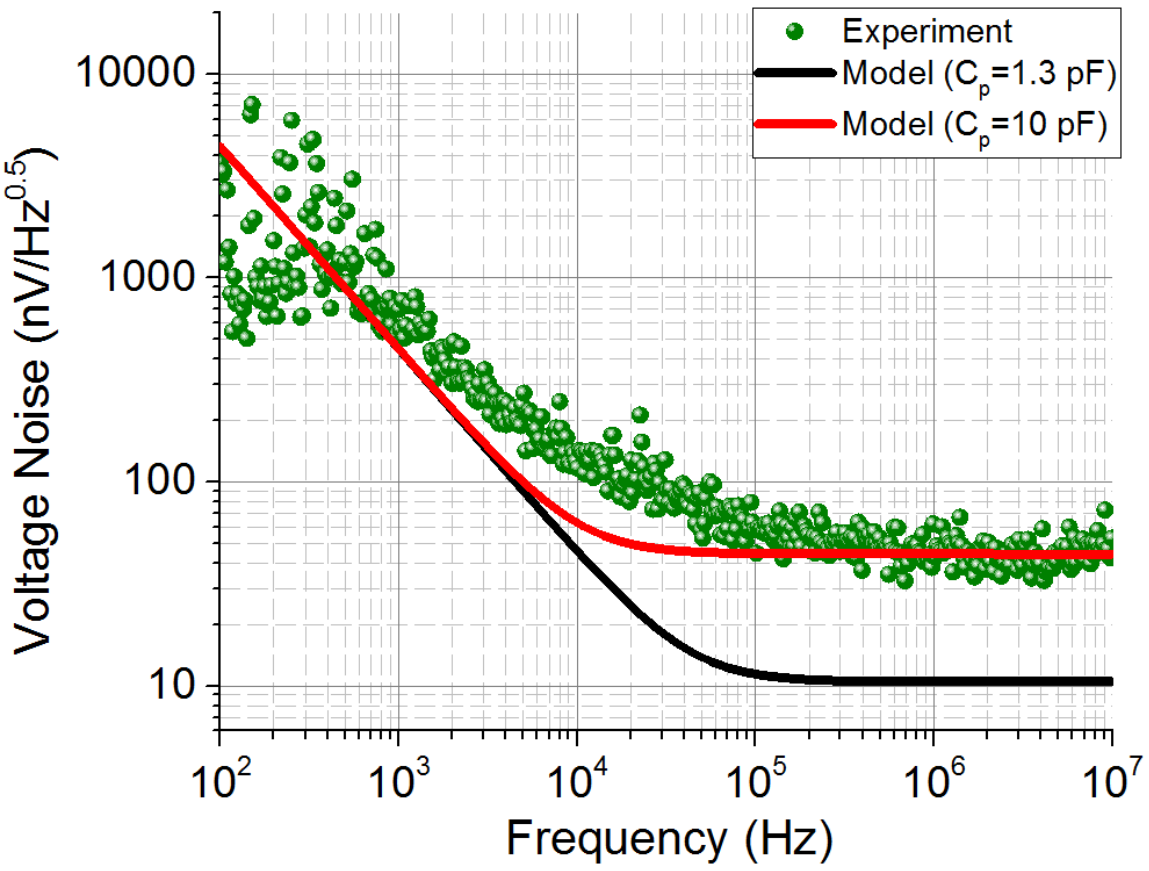

FIG. A.7 : Electrical noise spectrum. The low frequency is set at 100 kHz because of the 1/f corner of the AD4817 (only white noise is included in our model). The black line is the simulated noise for input capacitance equals to the amplifier input capacitance. The red line is a fit of the experimental noise floor (10 pF input capacitance). The discrepancy below 100 kHz likely occurs because of 1/f noise from amplifier which is not included in our model.

2. Down-mixing detection scheme

Heterodyne detection scheme has been used to overwhelmed parasitic capacitance. Indeed, as explained before, the capacitance change to be sensed would be in the order of several attofarads. A simple synchronous detection cannot be set-up here because of the high parasitic capacitance from connection paths, from 0.1 to 1 pF, depending on the design. Indeed, even if the capacitive actuation needs a half-omega signal to create an omega force, the unwanted small second harmonic of signal generator is enough to hide the useful signal.

For capacitive actuation and detection, two possibilities are offered for downmixing, depending on the term we want to use in the torque expression. As explained before the electrical torque and the output voltage (without parasitic signals) can be expressed as follows:

$$T_e = \frac{1}{2}\frac{\partial C}{\partial \theta}\tilde{U}^2$$
$$V_{out} = \frac{C(\theta)}{C_f}\widetilde{V_{pol}} \tag{A.39}$$

$\tilde{U}$ is the potential difference between the fixed and mobile electrode. One can observe that the output voltage would be proportional to the product between $\widetilde{V_{pol}}$ and T_e through the angle θ. Assuming the polarization voltage $\widetilde{V_{pol}} = V_{pol}\cos(\omega t - \Delta\omega)$ and an actuation voltage $\widetilde{V_{AC}} = V_{AC}\cos(\omega/2\, t)$, the torque will be:

$$T_e = 1/2\frac{\partial C}{\partial \theta}\left(V_{AC}\cos\left(\frac{\omega}{2}t\right) - V_{pol}\cos\big((\omega - \Delta\omega)t\big)\right)^2 \tag{A.40}$$

Expanding the square leads to 3 force terms:

$$T_e \propto \frac{V_{AC}^2}{2} + \frac{V_{pol}^2}{2} + \frac{V_{AC}^2}{2}\cos(\omega t) + \frac{V_{pol}^2}{2}\cos\Big(2\big((\omega - \Delta\omega)t\big)\Big) - V_{pol}V_{AC}\left(\cos\left(\left(\frac{3\omega}{2} - \Delta\omega\right)t\right) - \cos\left(\left(\frac{\omega}{2} - \Delta\omega\right)t\right)\right) \tag{A.41}$$

Force terms that do not depend on ω are filtered by the resonator. The output voltage will have the following expression:

$$V_{out} \propto T_e\widetilde{V_{pol}} \propto V_{pol}\frac{V_{AC}^2}{4}\big(\cos(\Delta\omega t) + \cos\big((2\omega - \Delta\omega)t\big)\big) \tag{A.42}$$

There is only one term depending on $\Delta\omega$. If $\Delta\omega$ is chosen small enough, a low pass filter placed after the lock-in instrument filters all the other frequencies, enhancing the dynamic range of the instrument.

In this case the force is only proportional to V_{AC}^2. We observe that our background is still affected by the voltage increase in order to drive the resonator to the onset of non-linearity. Therefore, we prefer another mode of downmixing as explained below.

For an actuation voltage at $\widetilde{V_{AC}} = V_{AC}\cos\big((2\omega - \Delta\omega)t\big)$, the useful force will be proportional to $V_{pol}V_{AC}$. This actuation mean is advantageous because a high bias voltage V_{pol} increases both the output voltage and the deflection angle. The actuation voltage V_{AC} can be lower than for $f/2$ actuation and therefore the signal to background ratio is improved.

The useful component in the output amplitude reads:

$$V_{out} = V_{pol}\frac{\big(\delta C(\theta_r) - \delta C(-\theta_r)\big)}{4C_{C2V}} \qquad \text{(A.43)}$$

The main drawback of this detection scheme is that half of the signal energy is lost in the high-frequency component which deteriorates the signal to noise ratio (*SNR*).

3. Noise analysis

Using the down-mixing scheme described above, spectral responses of several pixels are measured. In parallel, Allan deviations of such systems are achieved for different AC-actuation voltages to determine the noise floor level. We notice that the Allan deviations tend to a plateau whose origin is not perfectly known. If this noise corresponds to an amplitude noise, its level should decrease when increasing the output voltage at resonance (given Robin's relation [6]). The results of frequency stabilities when

increasing the signal amplitude at resonance is shown in

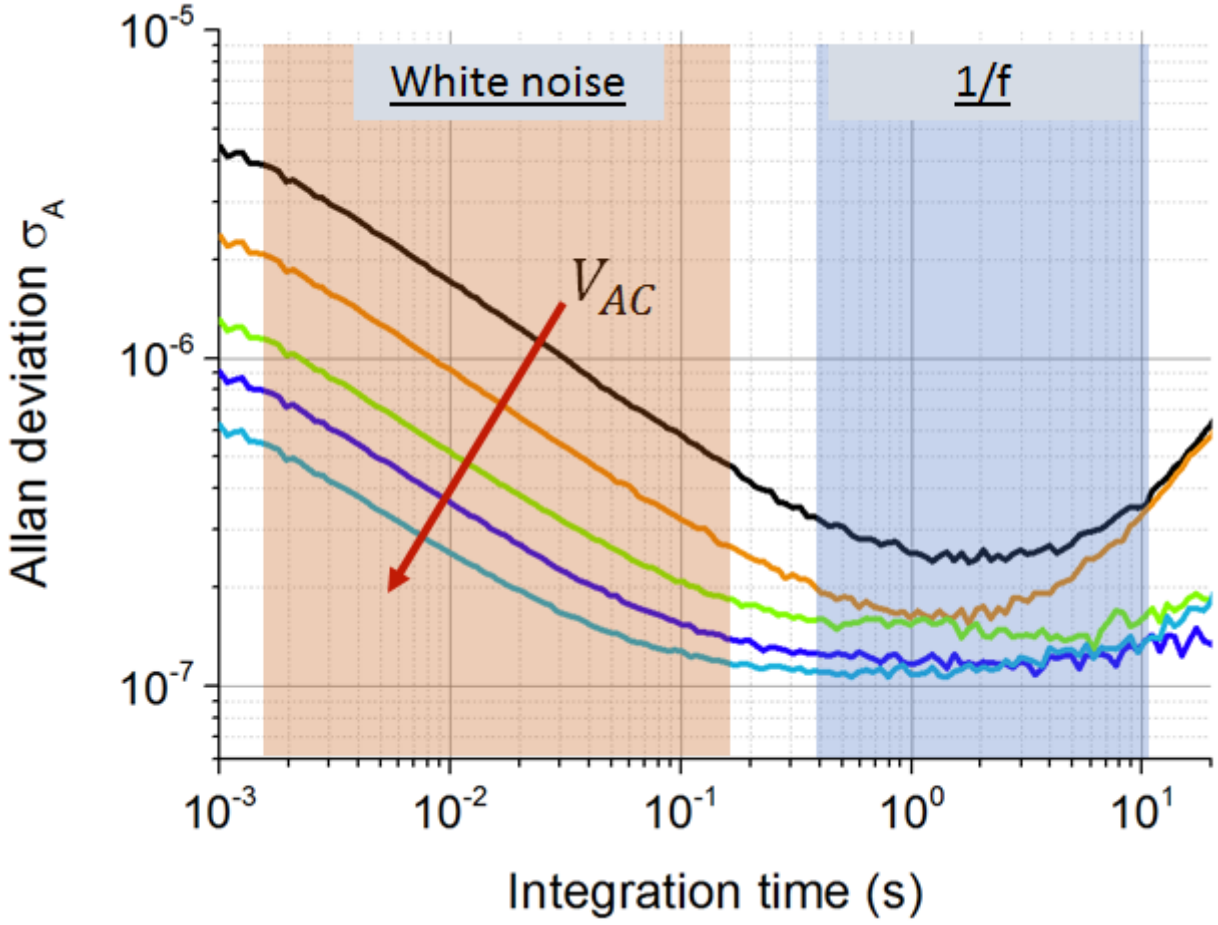

FIG. A.8. As expected by the experimental electronical noise, we observe an improvement in the frequency stability in the white noise region (slope=$\tau^{-1/2}$). On the contrary, this improvement is no longer observed as we reach higher integration time, and the plateau level.

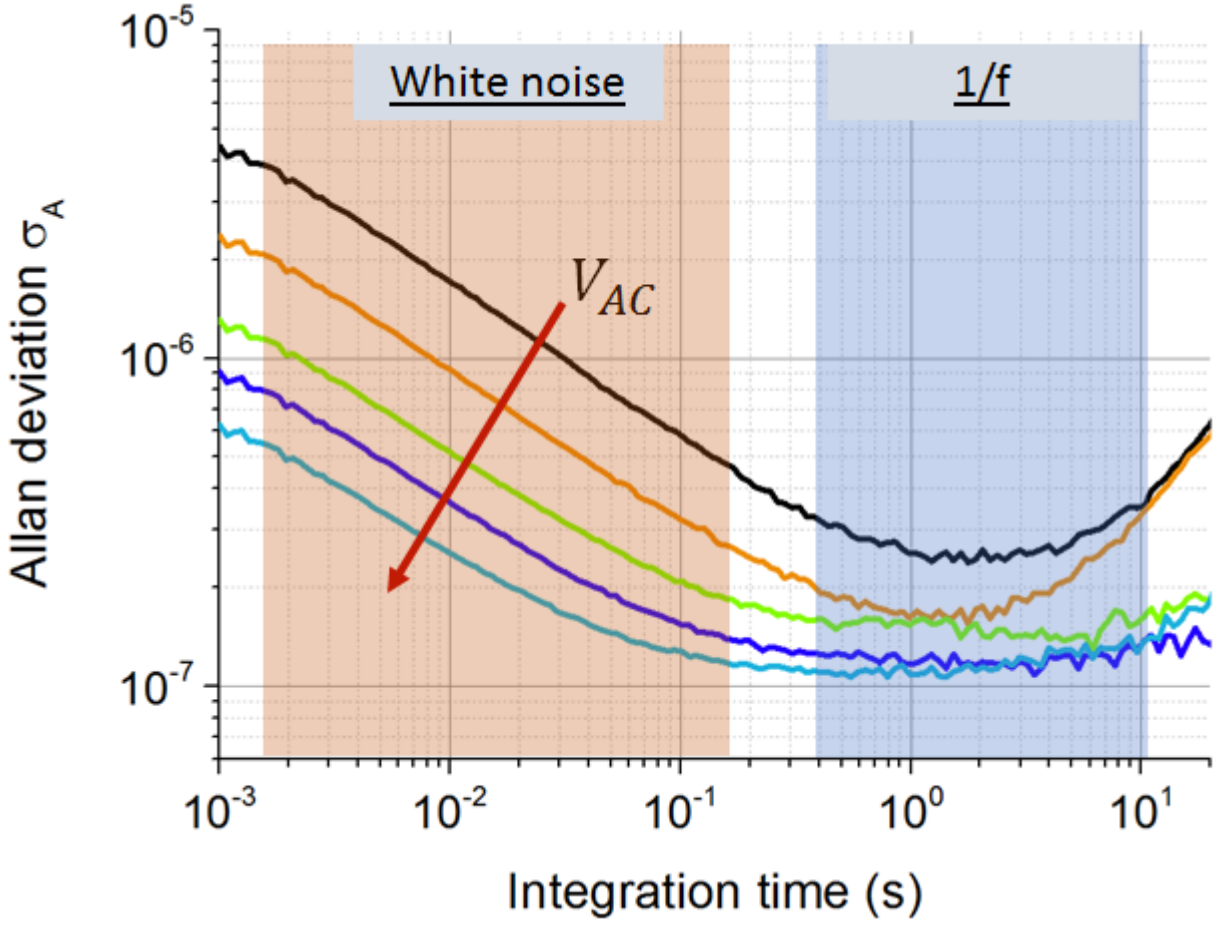

FIG. A.8 : Allan Deviation as function of integration time. We acquired the resonance frequency data in open loop for different actuation voltages from 0.3 V to the onset of non-linearity (1.4 V) for a polarization voltage of 10 V. Long terms drift occurs above 10 s. The white noise zone decreases significantly when improving the output signal at resonance. However, a plateau occurs over 20 ms, which is not improved when resonance amplitude is increased.

This fluctuation could be related to current fluctuations inside the resonator body due to a voltage noise through the arm electrical resistances. Therefore the actuation voltage fluctuations lead to local voltage difference – i.e. temperature fluctuations. In the same line, a displacement current occurs in the rods due to actuation voltage through the static capacitance C_0. We therefore measure the voltage noise of our generator for both actuation and polarization voltages to assess the frequency contribution of this potential noise source. It appears that the noise level of the polarization voltage is much higher than the

actuation voltage, especially because of its high amplitude (10V peak). We therefore focus on this signal. Considering $\widetilde{V_{pol}} = (V_{pol} + \delta V)\cos\big((\omega - \Delta\omega)t\big)$ and a symetric polarization of the paddle, the equivalent circuit for this capacitive current is sketched up on FIG. A.9:

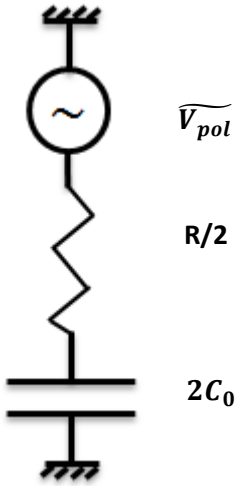

FIG. A.9: Equivalent electrical scheme for capacitive current from polarization voltage. The paddle is polarized symmetrically in order to avoid high static capacitive current due to parasitic capacitance inside one of the isolation rod. Therefore, the capacitive current sees an equivalent R/2 resistor – the measured resistance R between the two paddle pads is $\sim\mathbf{14}\ \boldsymbol{k\Omega}$. Then the paddle sees twice static capacitance $\boldsymbol{C_0}$ (actuation and detection electrode), which has been evaluated to $\mathbf{0.18}\ \boldsymbol{fF}$.

Then, the power dissipated inside the isolation rods is:

$$P_r = \frac{R}{2} 4 < C_0(\omega - \Delta\omega)\widetilde{V_{pol}} >^2 = R\big(C_0(\omega - \Delta\omega)\big)^2 (V_{pol}^2 + 2V_{pol}\delta V + \delta V^2) \qquad \text{(A.44)}$$

We remove the « static » term and only focus on the electrical noise contribution. Considering δV^2 as a second order term, the Joule heating fluctuations are:

$$P_r = 2R\big(C_0(\omega - \Delta\omega)\big)^2 V_{pol}\delta V \qquad \text{(A.45)}$$

For the sake of simplicity, we consider a long integration time (longer than thermal time response) and we assume that the torsional rods temperature profile is constant – it corresponds to the paddle temperature rise. Thus:

$$\sigma_A \sim \frac{2\alpha_T R}{G}\left(C_0(\omega - \Delta\omega)\right)^2 V_{pol}\sqrt{S_V} \tag{A.46}$$

At 1s integration time, with $C_0 = 0.15\ fF, f - \Delta f \sim 800\ kHz, R \sim 7\ k\Omega, G = 5 \times 10^{-8}\ W/K$ and $\alpha \sim -60\ ppm/°C$, we estimate the Allan deviation at $\sigma_A \sim 2 \times 10^{-18}$, which is much higher than 2×10^{-7}observed at 1s-integration time ($\sqrt{S_V} = 25\ nV/\sqrt{Hz}$).

4. Thermal measurement

Experimental set-up for IR power responsivity

We sketch up our set-up on FIG. A.10.

Since a black body is a lambertian source, its monochromatic luminance L_λ^0 (given by Planck's law) is constant over the field of view and the intensity is given by:

$$I = L^0 \cos(\theta)$$

$$L_\lambda^0 = \frac{2hc^2}{\lambda^5\left(e^{-\frac{hc}{k_B T\lambda}} - 1\right)} \tag{A.47}$$

Where λ is the wavelength, k_B the Boltzmann constant, T the temperature, h the Planck constant and c the speed of light. Finally, the µbolometer illumination is directly linked to the intensity:

$$E = \int_\theta^{\theta_m} L^0 \cos(\theta) d\Omega \tag{A.48}$$

Where dΩ is the solid angle under which the bolometer sees the blackbody $d\Omega = dA/d^2$, dA is the disk area of the disk comprised between θ and $\theta + d\theta$.

$$dA = 2\pi r dr \approx 2\pi \sin(\theta)\, d^2\, d\theta \text{ because } d\theta \sim dr/d \quad \text{(A.49)}$$

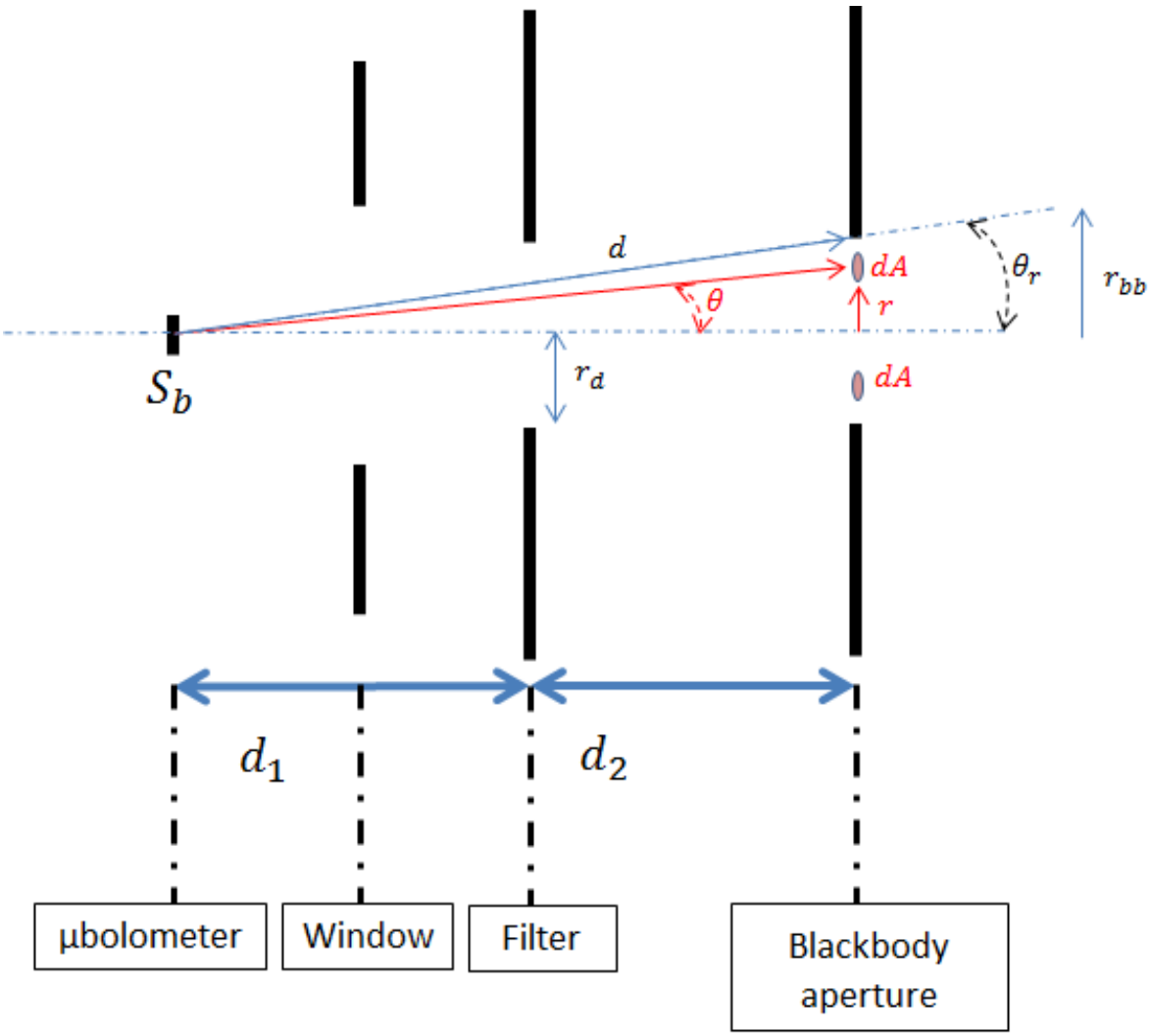

FIG. A.10: Radiometric scheme of infrared calibration. A Germanium is used to seal the vacuum chamber. Yet, a more performant filter is needed to accurately calibrate our sensor in the 8-14µm range. Indeed, since the detector is close to the source, atmospheric absorption is very low. In the chosen configuration, the sensor sees the whole blackbody aperture.

Finally, we get the incident energy:

$$P_0 = S_b \pi L^0 \sin^2(\theta_m) \tag{A.50}$$

θ_m depends on the configuration. If a diaphragm partially occults the blackbody aperture, the incident energy will only depend on the distance between the sensor and the diaphragm. In our case, the detector senses the entire area of the blackbody.

$$\begin{cases} \sin^2(\theta_m) = \dfrac{r_d^2}{r_d^2 + d_1^2} \text{ if limited by a diaphragm} \\ \sin^2(\theta_m) = \dfrac{r_{bb}^2}{r_{bb}^2 + (d_1 + d_2)^2} \text{ otherwise} \end{cases} \tag{A.51}$$

Finally, we calibrate the transmission coefficient of our experiment. We use a Fourier Transform Infrared Systems for characterizing our filter and window. Atmospheric absorption is neglected because of the small typical distances of our experiment.

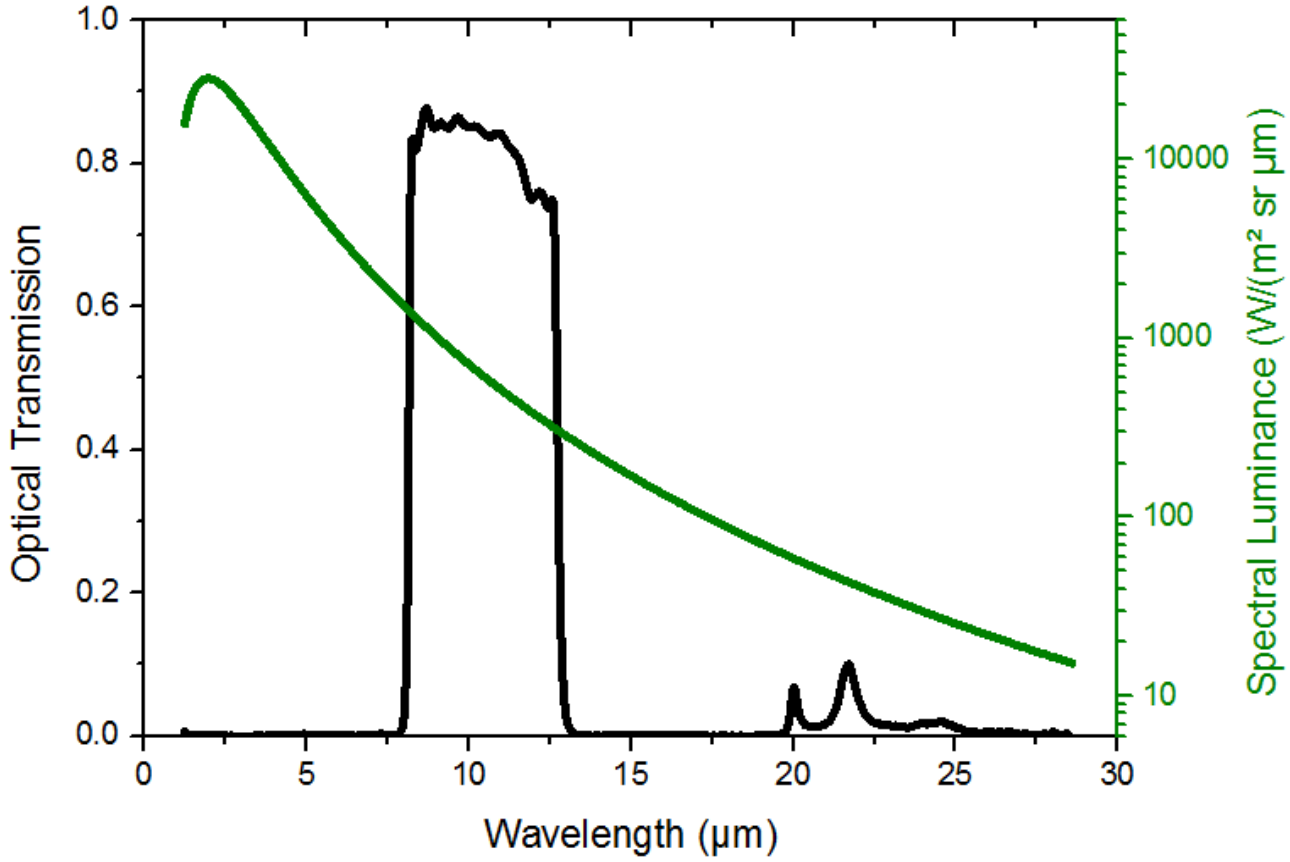

FIG.A.11 : Transmission coefficient of the Ge filter & window (black curve). The spectral luminance of a perfect blackbody at 1200 °C is also plotted (green curve). The surface under the curves intersections represents

the luminance seen by the detector inside the chamber.

For $d_1 = 2.2\ cm$ and $d_2 = 6.4\ cm$, the incident energy on bolometer surface is 26 nW for a temperature blackbody of 1200°C.

Temperature coefficient of frequency

The Temperature Coefficient of Frequency (*TCF*) α_T are measured for the different designs presented in the FIG. 1 of the manuscript. We do not observe significant differences on technological process for these three designs (TiN low stress & stiffer SiN have also been deposited).

The Temperature Coefficient of Young Modulus for crystalline silicon (resp SiN) is -70 ppm/°C (resp 48 ppm/°C). Therefore a *TCF* of -35 ppm/°C (resp -24 ppm/°C) is expected in the absence of thermal strain.

FIG. A.12 presents both measured *TCF* for these devices and a Figure of Merit to compare them in terms of performance for bolometric applications. We choose a Figure of Merit which is the product of the maximum linear output amplitude at resonance, the quality factor, the *TCF*, the absorption and the thermal resistance.

The flexural resonance in a "butterfly" design is also studied. One would expect a greater (and positive) *TCF* because of thermal stress influences. However, we do not observe such performance and, the low V_{out} observed doesn't make it suitable for IR sensing.

Thus, it seems that thermal strain effectively plays a role in the *TCF*. However, instead of hardening the torsion bar, we believe that an enhancement of the negative effect on resonance is caused by an increase of the inertia moment of the structure. FEM simulations show a positive coefficient on temperature for inertia moment and are in good agreement with the observation. Notice that these simulations highly depend on residual stress, and it is still an issue to obtain quantitative simulation results.

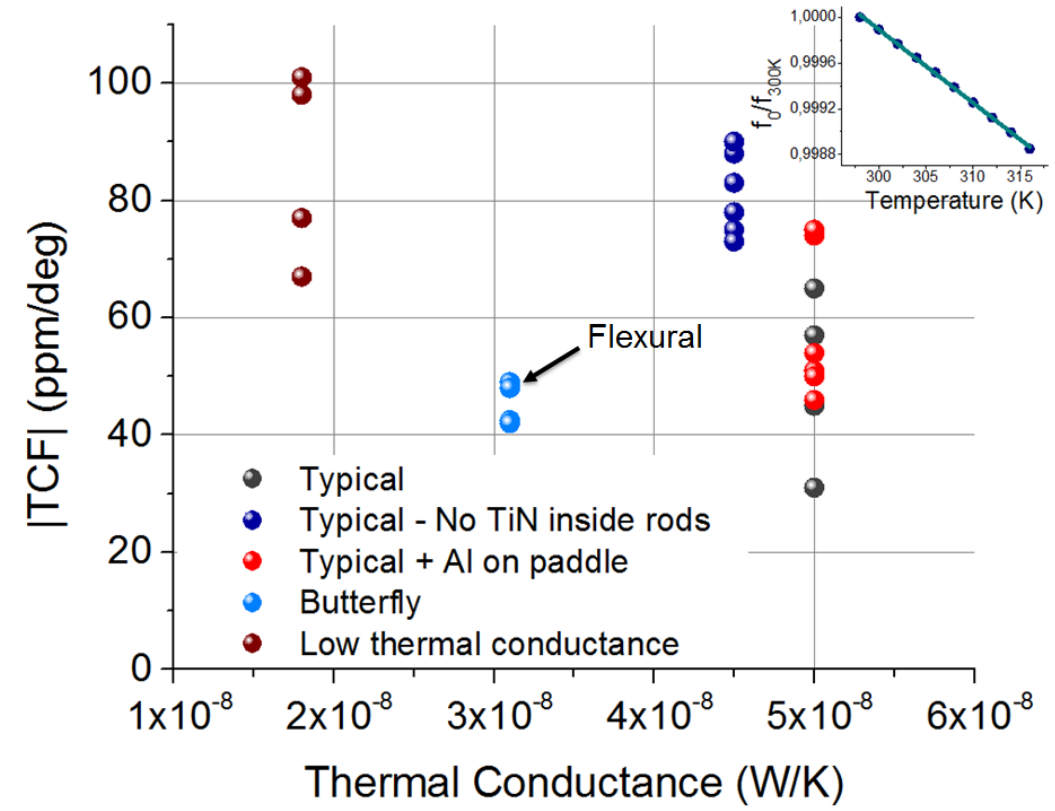
|TCF| (ppm/deg)
Thermal Conductance (W/K)
Flexural
Typical
Typical - No TiN inside rods
Typical + Al on paddle
Butterfly
Low thermal conductance
f0/f300K
Temperature (K)

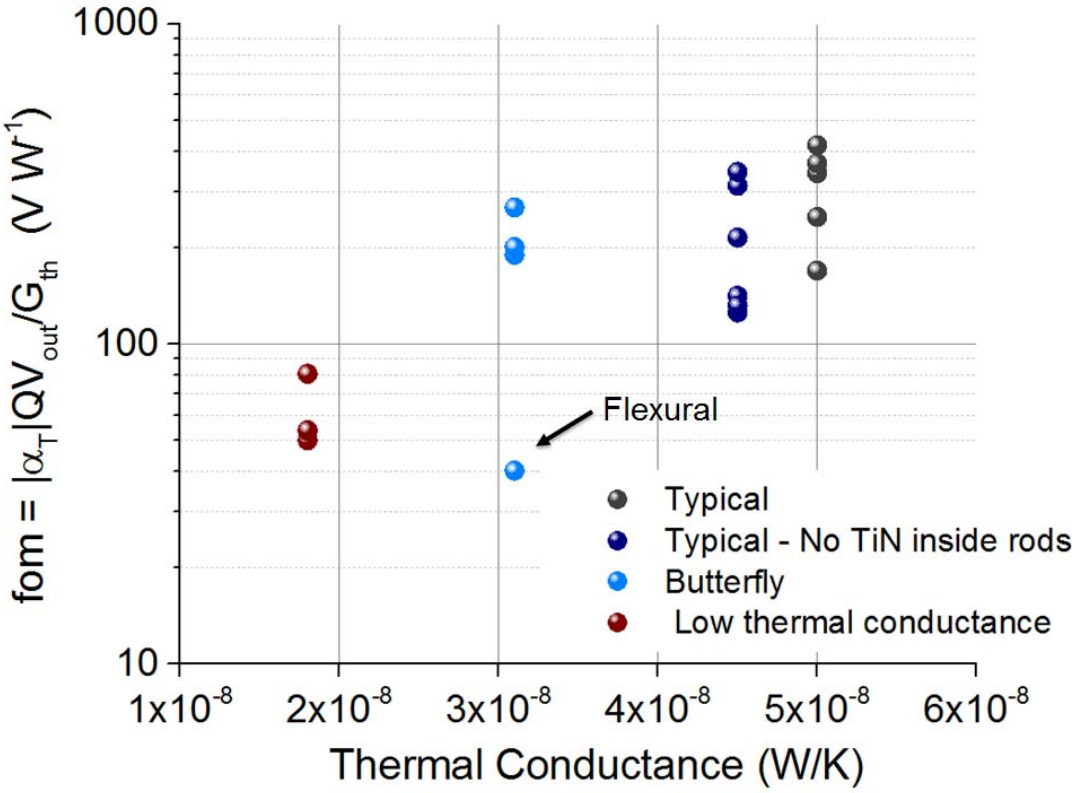
fom = |αT|QVout/Gth (V W-1)
Thermal Conductance (W/K)
Flexural
Typical
Typical - No TiN inside rods
Butterfly
Low thermal conductance

FIG. A.12 : <u>Top:</u> TCF as function of thermal conductance. Typical devices are similar to Fig. 1. Devices withoutt TiN inside rods have also been tested. Blind pixels with 300 nm-thick Al on top of the paddle were designed. <u>Inset:</u> Typical results from a TCF measurement over 20 °C. **<u>Bottom:</u>** $\boldsymbol{FOM = \eta \times V_{out} \times Q \times |TCF|/G_{th}}$ **as function of thermal conductance.** It appears that typical pixels performances are the highest among all devices, especially because of their high output voltage.

Thermal time response

The response time is measured thanks to Helium Neon laser from commercial Polytech vibrometer [7]. Indeed, the rising time of optical signal from commercial choppers is not fast enough to measure the response time of our device. This experiment is conducted in Open Loop scheme and the optical power is set in order to stay in the linear region ($\pm$ 20°). We use a 10-90 % method to extract the fall time t_r, and therefore the response time of the first order low-pass filter τ ($\tau = t_r/\ln(9)$). With this method, we extract a time response of 430 µs, which is close to the 500 µs expected by thermal equations for our design.

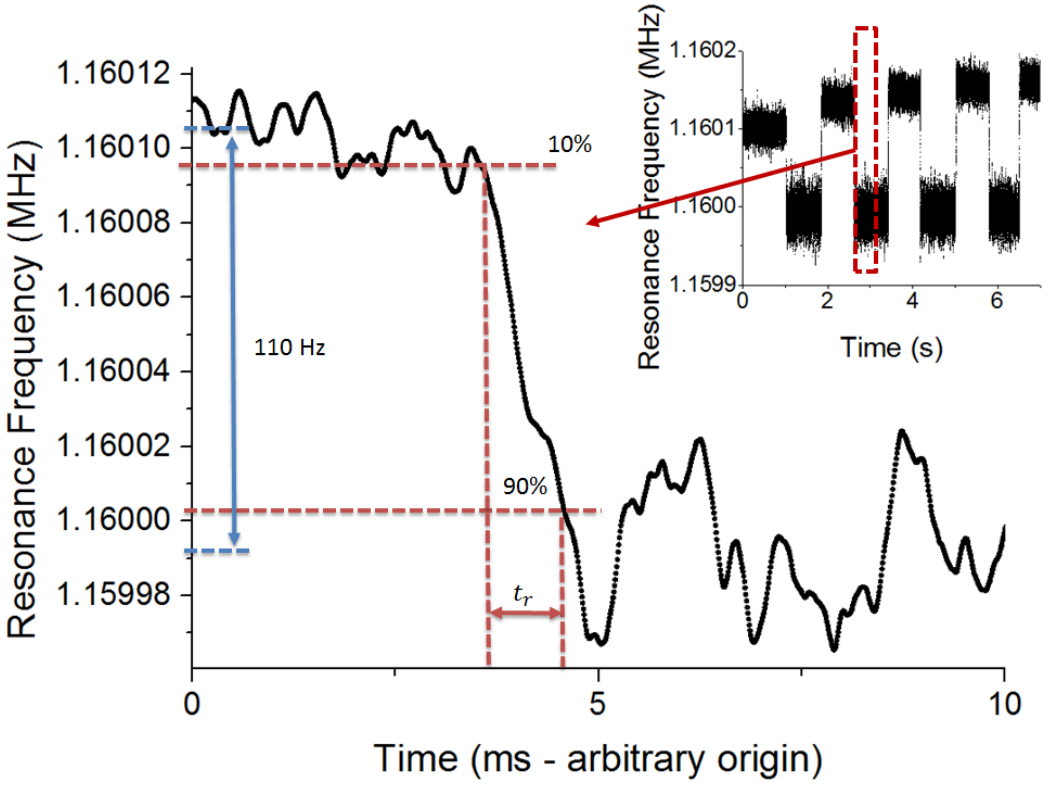

FIG. A.13 : Resonance frequency as a function of acquisition time. A 1 mW (attenuated by a factor $\mathbf{2^7}$ with an optical dimmer) red laser is focused on the active pixel. The resonance frequency in real time from phase data at resonance using Robbin's relation. An effective integration time of 180 µs is used. We verified that the response time is not limited by electrical low-pass filter from our lock-in by testing $\boldsymbol{\tau} = 50$ µs. Obviously, the noise was increased, but the response time was found to be similar. **Insert:** Full data from our response time measurement. The average frequency jump is estimated to 110 Hz. Then, the response time is extracted from one event fall time (red).

REFERENCES

[1] P. W. Kruse and D. D. Skarud, Uncooled Infrared Imaging Arrays and Systems, Willardson Weber., vol. 47. Academic Press (1997).

[2] D. Antonio, H. Pastoriza, P. Julian, and P. Mandolesi, Cryogenic transimpedance amplifier for micromechanical capacitive sensors, Rev. Sci. Instrum., vol. 79, no. 8, pp. 084703-084703-5, (2008).

[3] Analog Devices, Op Amp Total Output Noise Calculations for Second-Order System, http://www.analog.com/media/en/training-seminars/tutorials/MT-050.pdf.

[4] Analog Devices, Low Noise, 1 GHz FastFET Op Amps, ADA4817-1/ADA4817-2, http://www.analog.com/media/en/technical-documentation/data-sheets/ADA4817-1_4817-2.pdf.

[5] Z. Hu, H. Quan, F. Zhang, and P. Wang, Ultra-Low Noise Charge Sensitive Amplifier for MEMS Gyroscope, Fifth International Conference on MEMS, NANO, and Smart Systems (ICMENS), (IEEE, Dubai, 2009) pp. 29–32.

[6] W. P. Robins, Phase Noise in Signal Sources: Theory and Applications, IET, (1984)

[7] P. GmbH, Polytec: OFV-55x Fiber-Optic Sensor Head [Online]. Available: http://www.polytec.com/eu/products/vibration-sensors/single-point-vibrometers/modular-systems/ofv-55x-fiber-optic-sensor-head/.